

# Template-Assisted Synthesis of Honeycomb-Like CoFe<sub>2</sub>O<sub>4</sub>/CNTs/rGO Composite as Anode Material for Li/Na-Ion Batteries

Min Zhao,<sup>[a]</sup> Jian Xiong,<sup>[a]</sup> Yang Yang,<sup>\*,[b]</sup> and Jinbao Zhao<sup>\*,[a]</sup>

CoFe<sub>2</sub>O<sub>4</sub> is a fascinating anode material due to its high theoretical capacity. However, the low electronic conductivity, limited electrochemical kinetics and huge volume expansion lead to poor electrochemical performance. Here, the CoFe<sub>2</sub>O<sub>4</sub>/CNTs/rGO ternary composite with a honeycomb-like structure (PS-CFO/CNTs/rGO) has been synthesized via a spray drying method assisted by polystyrene (PS) soft template. The rational 3D porous structure design not only enhances the transport capacity of Li/Na ions, but also provides buffer spaces for alleviating volume expansion, resulting in rapid electrochemical

kinetics and improved electrode integrity during cycling. In particular, to improve the electrochemical performance, a facile pre-treatment process combining heat-treatment and pre-sodiation treatment is first developed for the anode materials of sodium-ion batteries (SIBs). As a result, at 1 A g<sup>-1</sup> after 365 cycles, the pronounced capacity of PS-CFO/CNTs/rGO composite can be maintained at 750 mAh g<sup>-1</sup> for lithium-ion batteries (LIBs), and after 5000 cycles, maintained at 195 mAh g<sup>-1</sup> for the SIBs.

## 1. Introduction

Nowadays, since the lithium-ion batteries (LIBs) were commercialized successfully, they have been widely used in our daily life.<sup>[1]</sup> Owing to the characteristics such as no pollution, longer cycling life, and higher working voltage,<sup>[2]</sup> the LIBs have dominated the market of portable devices and electric vehicles.<sup>[3]</sup> However, the difficult recycling of waste batteries and the scarcity of Li resource also should be taken into account.<sup>[4]</sup> To solve this problem, many researchers have attempted to develop new battery systems by using the reserve-richer and cheaper materials.<sup>[5]</sup> In the constant search, both Na and Li, as the alkali metal elements in the periodic table, are found to have similar chemical properties.<sup>[6]</sup> Moreover, the sodium is an abundant element, and is also very cheap due to the easy extraction from seawater.<sup>[7]</sup> Due to the above-mentioned advantages, the sodium ion batteries (SIBs) have been considered a promising candidate in the development of energy storage system after the LIBs.<sup>[8]</sup> Therefore, the current research focus is to find the suitable active materials.<sup>[9]</sup>

Among the potential anode materials, because of the advantage of higher discharge capacities than the conventional carbon anode materials for LIBs and SIBs, the transition metal oxides (TMO) have gained more attentions.<sup>[10]</sup> However, the bulk materials of these traditional binary TMO, such as Co<sub>3</sub>O<sub>4</sub>,<sup>[11]</sup> Fe<sub>3</sub>O<sub>4</sub>,<sup>[12]</sup> Mn<sub>3</sub>O<sub>4</sub>,<sup>[13]</sup> have some drawbacks like low electrical conductivity. And now, in order to overcome the shortcomings of simple binary oxides, the ternary metal oxides have been studied extensively.<sup>[14]</sup> Due to the high dielectric constant, and active electronic transport capacity, the ternary metal oxides possess higher electronic conductivity compared to the binary metal oxides generally. Moreover, the multiple adjustable valence state of ternary metal oxides provides abundant electrochemical active sites.

Among those potential ternary metal oxides, due to the high theoretical capacity of 916 mAh g<sup>-1</sup>, the spinel ferrite CoFe<sub>2</sub>O<sub>4</sub><sup>[14]</sup> has become a good candidate for both LIBs and SIBs.<sup>[15]</sup> However, there are still some obstacles that prevent its practical application. One is its limited electronic conductivity compared to carbon materials, and other is the huge volumetric expansion during the cycling. In order to overcome these obstacles, the carbon coating and morphology modification are usually adopted. Xia et al.<sup>[16]</sup> reported a CoFe<sub>2</sub>O<sub>4</sub>-graphene nanocomposite synthesized via hydrothermal method, and it manifested a high discharge capacity. Alok et al.<sup>[17]</sup> reported a Co<sub>3</sub>O<sub>4</sub>/CoFe<sub>2</sub>O<sub>4</sub> nanocomposite prepared by urea-assisted auto-combustion strategy, and after 60 cycles, the reversible capacity is maintained at 896 mAh g<sup>-1</sup>. Although the relative higher cycling capacity has been achieved, the high rate stability and long-term cycling performance are still needed to improve.

Herein, we have synthesized the CoFe<sub>2</sub>O<sub>4</sub>/carbon nanotubes/reduced graphene oxide ternary composite via polystyrene (PS) soft template-assisted spray drying method (denoted as PS-CFO/CNTs/rGO) for LIBs and SIBs as the anode material.

[a] M. Zhao, J. Xiong, Prof. J. Zhao  
State-Province Joint Engineering Laboratory of Power Source Technology for New Energy Vehicle, Engineering Research Center of Electrochemical Technology, Ministry of Education, College of Chemistry and Chemical Engineering  
Xiamen University, Xiamen,  
361005, P.R. China  
E-mail: jbzha@xmu.edu.cn

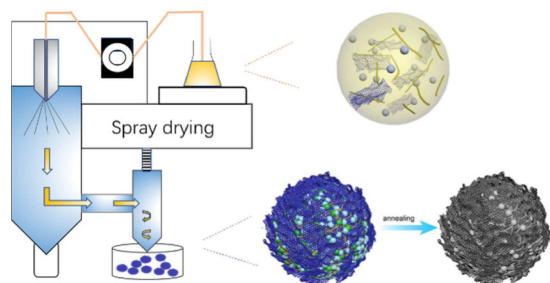
[b] Y. Yang  
School of Chemical Engineering and Light Industry  
Guangdong University of Technology  
Guangzhou 510006, China  
E-mail: yangyang@gdut.edu.cn

Supporting information for this article is available on the WWW under <https://doi.org/10.1002/celc.201900800>

Due to the rational microstructure design and introduction of conductive carbon, the above thorny problems can be overcome effectively: (1) The  $\text{CoFe}_2\text{O}_4$  is coated with rGO to avoid its direct exposure to electrolyte. (2) The CNTs constitute a 3D conducting network, which can improve the electrical conductivity of the composite. (3) The diffusion path of  $\text{Li}^+$  can be shortened due to the hollow porous structure of the composite, and a mass of interspace also can relieve the volume effect. In addition, a facile pre-treatment route combining heat-treatment and pre-sodiation treatment has also been developed successfully to further enhance the initial coulombic efficiency (ICE) and cycling stability of PS-CFO/CNTs/rGO composite for SIBs. Consequently, the PS-CFO/CNTs/rGO composite exhibits excellent electrochemical properties.

## 2. Results and Discussion

As shown in the Scheme 1, the precursor aqueous solution containing  $\text{Fe}(\text{NO}_3)_3$ ,  $\text{Co}(\text{NO}_3)_2$ , CNTs, GO and PS microspheres is



Scheme 1. Synthesis diagram of PS-CFO/CNTs/rGO composite.

pumped into the spray nozzle. Due to the high temperature in the vessel, the solvent inside the ejected droplet rapidly evaporates, thus forming a hollow ball structure. Then the obtained material is transferred into the tubular furnace annealing under the atmosphere of Ar at  $600^\circ\text{C}$  for 10 h. And PS microspheres are depolymerized and removed in this process, so as to obtain the PS-CFO/CNTs/rGO composite with honeycomb-like structure. For comparison, the pristine  $\text{CoFe}_2\text{O}_4$  (denoted as Pure CFO),  $\text{CoFe}_2\text{O}_4/\text{CNTs}$  (denoted as CFO/CNTs),  $\text{CoFe}_2\text{O}_4/\text{rGO}$  (denoted as CFO/rGO),  $\text{CoFe}_2\text{O}_4/\text{rGO}/\text{CNTs}$  (denoted as CFO/CNTs/rGO) are synthesized in the absence of corresponding carbon materials and PS emulsion solution under the same preparation process.

Figure 1a show the XRD curves of Pure CFO, CFO/CNTs and PS-CFO/CNTs/rGO composites. All the peaks of three samples are consistent with the PDF standard pattern of  $\text{CoFe}_2\text{O}_4$  (JCPDS No. 01-079-1744). There is some impurity assigned to the metallic Co in the PS-CFO/CNTs/rGO composite (marked with \*), and it is reported that the existence of Co metal is beneficial to the improvement of electrical conductivity.<sup>[18]</sup> And the weak peak around  $26.2^\circ$  can be assigned to the CNTs and rGO.

The Raman spectrum (Figure 1b) of pristine  $\text{CoFe}_2\text{O}_4$  mainly shows five peaks located at 198, 296, 471, 602, and  $693\text{ cm}^{-1}$ ,

respectively.<sup>[19]</sup> The T-site mode is manifested in the bands at  $602\text{ cm}^{-1}$  and  $693\text{ cm}^{-1}$ , reflecting the local lattice effect of tetrahedral sublattice. Obviously, the O-site mode is reflected at 198, 296,  $471\text{ cm}^{-1}$ , corresponding to the octahedral sublattice.<sup>[20]</sup> These modes are assigned to the typical cubic anti-spinel structure of  $\text{CoFe}_2\text{O}_4$ . For the PS-CFO/CNTs/rGO and CFO/CNTs composites, two main peaks near  $1351\text{ cm}^{-1}$  and  $1599\text{ cm}^{-1}$  correspond to the D-band (defect-induced) and G-band (graphitic-induced), respectively.<sup>[21]</sup> The  $I_D/I_G$  ratio of PS-CFO/CNTs/rGO is 0.98, implying a relative high degree of crystallinity and graphitization of rGO and CNTs. Besides, the peaks of  $\text{CoFe}_2\text{O}_4$  can still be detected in the CFO/CNTs composite, which are hardly observed in the PS-CFO/CNTs/rGO composite. This is because the  $\text{CoFe}_2\text{O}_4$  particles in the PS-CFO/CNTs/rGO composite are well coated by a dual carbon protective layer (CNTs and rGO), and the laser signal is almost completely obscured by carbon materials. To further explore the content of carbon material in this composite, the thermogravimetric analysis (TGA) is conducted in air atmosphere (Figure S1a). When heated to  $800^\circ\text{C}$ , the final weight retention is 75%, meaning that the content of carbon material is 25%. In addition, in order to further measure the contents of each component in the composite, the TGA measurements of CNTs, GO and PS are performed in Ar atmosphere at the same heating rate (Figure S1). And it turns out that residual weight ratios are 100% (CNT), 47% (rGO) and 0% (PS). And for PS-CFO/CNTs/rGO composite, the proportions of CNTs and rGO are 15.75% and 9.25%.

XPS measurements are taken to further analyze the composition of the PS-CFO/CNTs/rGO composite. In the wide-scan spectrum of PS-CFO/CNTs/rGO composite (Figure S2a), there are prominent peaks of Fe 3p, C 1s, O 1s, Fe 2p and Co 2p. In addition, the high-resolution XPS spectra of Fe 2p and Co 2p are displayed in Figure 1c and d. The peaks located at 724.2 eV and 710.5 eV are related to Fe  $2p_{1/2}$  and Fe  $2p_{3/2}$ , respectively (Figure 1c). And the peaks at 780.2 eV and 784.6 eV correspond to Co  $2p_{3/2}$ , while the peaks at 795.8 eV and 802.6 eV belong to Co  $2p_{1/2}$  (Figure 1d). And the fitting results of these two spectra show that the Fe exists in the form of  $\text{Fe}^{3+}$ , while Co exists in the form of  $\text{Co}^{2+}$ .<sup>[10a,22]</sup> The C 1s high-resolution XPS spectra of the CFO/CNTs/rGO and the CFO/CNTs electrodes are shown in Figure S2b and c. The relative peak area ratio of the oxygen-containing bond (C–O and C=O) to C–C bond of the CFO/CNTs/rGO composite electrode (0.96) is larger than that of the CFO/CNTs composite electrode (0.40), which confirms the existence of rGO.<sup>[23]</sup> Based on the one-dimensional conductive network constructed by CNTs, rGO constructs two-dimensional surface conduction, which makes the composite constitute a 3D conductive system, and further alleviates the volume expansion of metal oxides.

The SEM and TEM images (Figure 2) show the morphology of PS-CFO/CNTs/rGO composite. In Figure 2a, the spherical hollow particles show the size distribution of 2–6  $\mu\text{m}$ . Figure 2b reveals the constituent details of the microsphere, the CNTs are wrapped and interwoven inside hollow microsphere. And the plenty of holes are also found due to the removal of PS template. Figure 2e show the TEM image of a single particle,

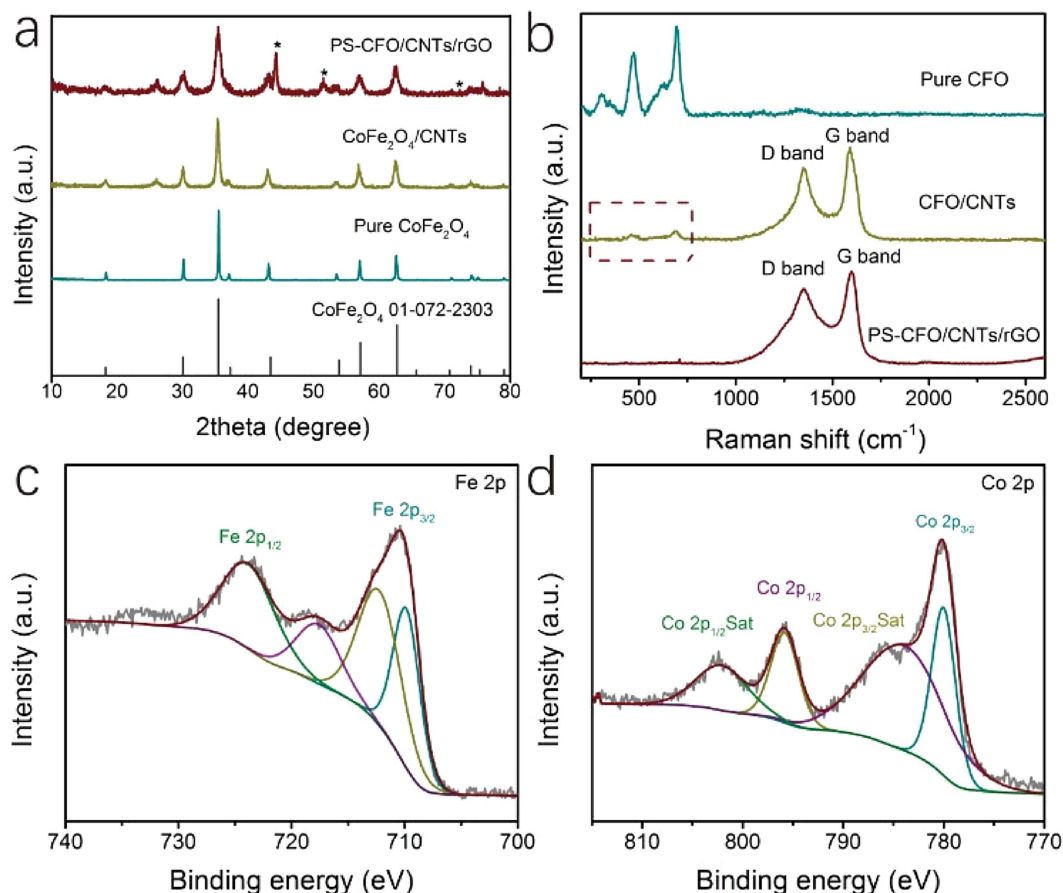


**Figure 1.** (a) XRD patterns and (b) Raman spectra of Pure CFO, CFO/CNTs and PS-CFO/CNTs/rGO composites; High-resolution XPS spectra of (c) Fe 2p and (d) Co 2p of PS-CFO/CNTs/rGO composite.

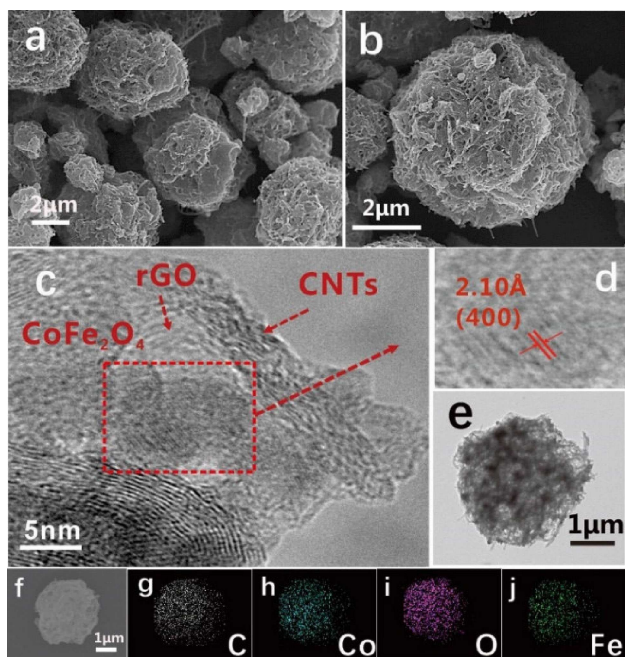


**Figure 2.** (a, b) SEM and (c–e) TEM images of the PS-CFO/CNTs/rGO microspheres; (f–j) Element mapping of a single PS-CFO/CNTs/rGO microsphere.

the large number of bright spots in the middle further corroborates the hollow porous structure of the composite. This porous structure shortens the diffusion path of Li<sup>+</sup> and alleviates the volume expansion effect effectively. The HRTEM image (Figure S3) shows that the CoFe<sub>2</sub>O<sub>4</sub> particles are connected to each other through CNTs forming a complete conductive skeleton. Figure 2c shows the lattices of three materials respectively. Among them, the curved lattices are attributed to CNTs and rGO, and the marked square area is the lattice of CoFe<sub>2</sub>O<sub>4</sub>. It also shows the tight connection of CoFe<sub>2</sub>O<sub>4</sub>, CNTs and rGO in the composite. Figure 2d shows the HRTEM image of the marked square area in Figure 2c, It displays clear crystal planes with a d-spacing of 0.21 nm, which is assigned to the (400) planes of CoFe<sub>2</sub>O<sub>4</sub>.<sup>[24]</sup> Figure 2f–j show the elemental mapping images, indicating the uniform distributions of C, Co, O and Fe. In order to further prove the rationality of this honeycomb structure, Figure S4 shows the SEM images of the other four samples for comparison.

The Nitrogen adsorption-desorption isotherms of PS-CFO/CNTs/rGO, CFO/CNTs and Pure CFO composites are shown in Figure 3. The nitrogen adsorption isotherm of PS-CFO/CNTs/rGO (Figure 3a) exhibits obvious type IV plot, showing that the composite has a porous structure. As for the pore-size distribution (Figure 3b) of PS-CFO/CNTs/rGO, there is an

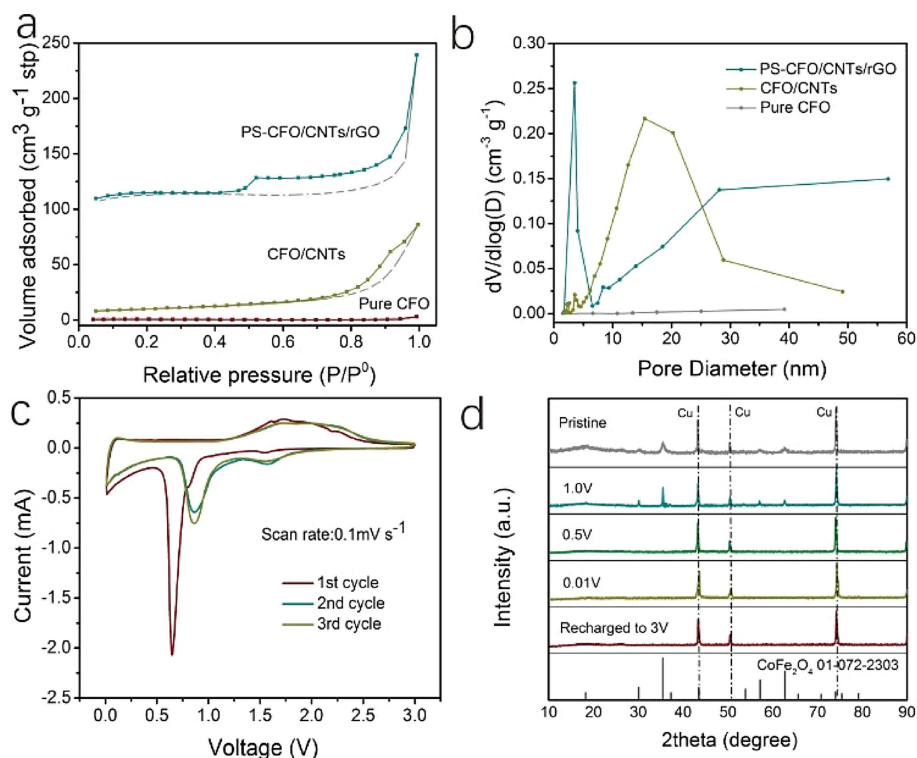
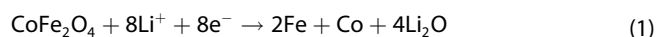


**Figure 3.** (a)  $N_2$  adsorption-desorption isotherms and (b) pore size distributions of Pure CFO, CFO/CNTs and PS-CFO/CNTs/rGO composites. (c) cyclic voltammogram curves of PS-CFO/CNTs/rGO composite. (d) The XRD patterns of different intercalation and deintercalation processes states of  $CoFe_2O_4$  electrode.

intensive peak near 4.0 nm, which is considered to be the mesoporous structure formed by both rGO and CNTs, while the wide peak at  $\sim 30$  nm is assigned to the removal of PS template, indicating that the PS-CFO/CNTs/rGO composite possesses a porous structure. The surface area of the PS-CFO/CNTs/rGO composite is measured to be  $348.2 \text{ m}^2 \text{ g}^{-1}$  with the pore volume of  $0.37 \text{ cm}^3 \text{ g}^{-1}$ , which is much higher than that of the Pure CFO ( $1.6 \text{ m}^2 \text{ g}^{-1}$ , and  $0.004895 \text{ cm}^3 \text{ g}^{-1}$ ), and CFO/CNTs ( $33.4 \text{ m}^2 \text{ g}^{-1}$ , and  $0.13 \text{ cm}^3 \text{ g}^{-1}$ ). It has been reported that the larger specific surface area can improve the contact between electrode and electrolyte.<sup>[22b]</sup>

Figure 3c shows the CV curves of PS-CFO/CNTs/rGO composite. In the initial cathodic process, the sharp peak at 0.68 V corresponds to the reduction of  $Fe^{3+}$  and  $Co^{2+}$ , and the formation of solid electrolyte interphase (SEI) layer with the partial decomposition of electrolyte. The two cathodic peaks at 0.89 V and 1.55 V in the following cycles correspond to the reduction reactions of  $Fe_2O_3$  and CoO, respectively.<sup>[25]</sup> The two anodic peaks observed at 1.61 V and 1.72 V are attributed to the oxidation reactions of the metallic Fe and Co. The electrochemical reaction equations of the initial cycle are expressed as follows (Eq. 1 and 2):



In subsequent cycles, the CV curves are basically coincident, showing the superior electrochemical reversibility. According to the above analysis, the  $CoFe_2O_4$  particles converts into a mixture of CoO and  $Fe_2O_3$  after the initial cycle, and the equation 3 above shows the electrochemical process after the initial cycle.

The reaction mechanism at initial cycle of  $CoFe_2O_4$  electrode is shown in Figure 3d. When the  $CoFe_2O_4$  electrode is discharged to 1.0 V, the peak positions of XRD patterns hardly change, which proves that there is no obvious phase change and electrochemical reaction before the discharge voltage above 1.0 V. However, when discharged to 0.5 V and 0.01 V, the characteristic peaks of  $CoFe_2O_4$  nearly disappear, resulting from the conversion of crystalline  $CoFe_2O_4$  to amorphous  $Li_2O$ , Co and Fe. After the initial charge process (recharged to 3.0 V), the XRD patterns exhibit no obvious peaks, which may be attributed to the formation of amorphous CoO and  $Fe_2O_3$ .<sup>[26]</sup>

Figure 4a and 4b show the typical charge-discharge profiles of PS-CFO/CNTs/rGO and Pure CFO composites at  $0.2 \text{ Ag}^{-1}$ . The initial discharge capacity of PS-CFO/CNTs/rGO is  $1484 \text{ mAh g}^{-1}$ , which is greater than that of Pure CFO ( $922 \text{ mAh g}^{-1}$ ). And the ICE of PS-CFO/CNTs/rGO is 73%, slightly lower than that of Pure CFO (80%), which may be due to the irreversible capacity brought by CNTs and rGO. In addition, in the first discharge process of PS-CFO/CNTs/rGO electrodes, we can see a voltage plateau at 0.68 V, which corresponds to the conversion reaction process mentioned above. Figure 4c investigates the cycle performances of the PS-CFO/CNTs/rGO, CFO/CNTs and Pure

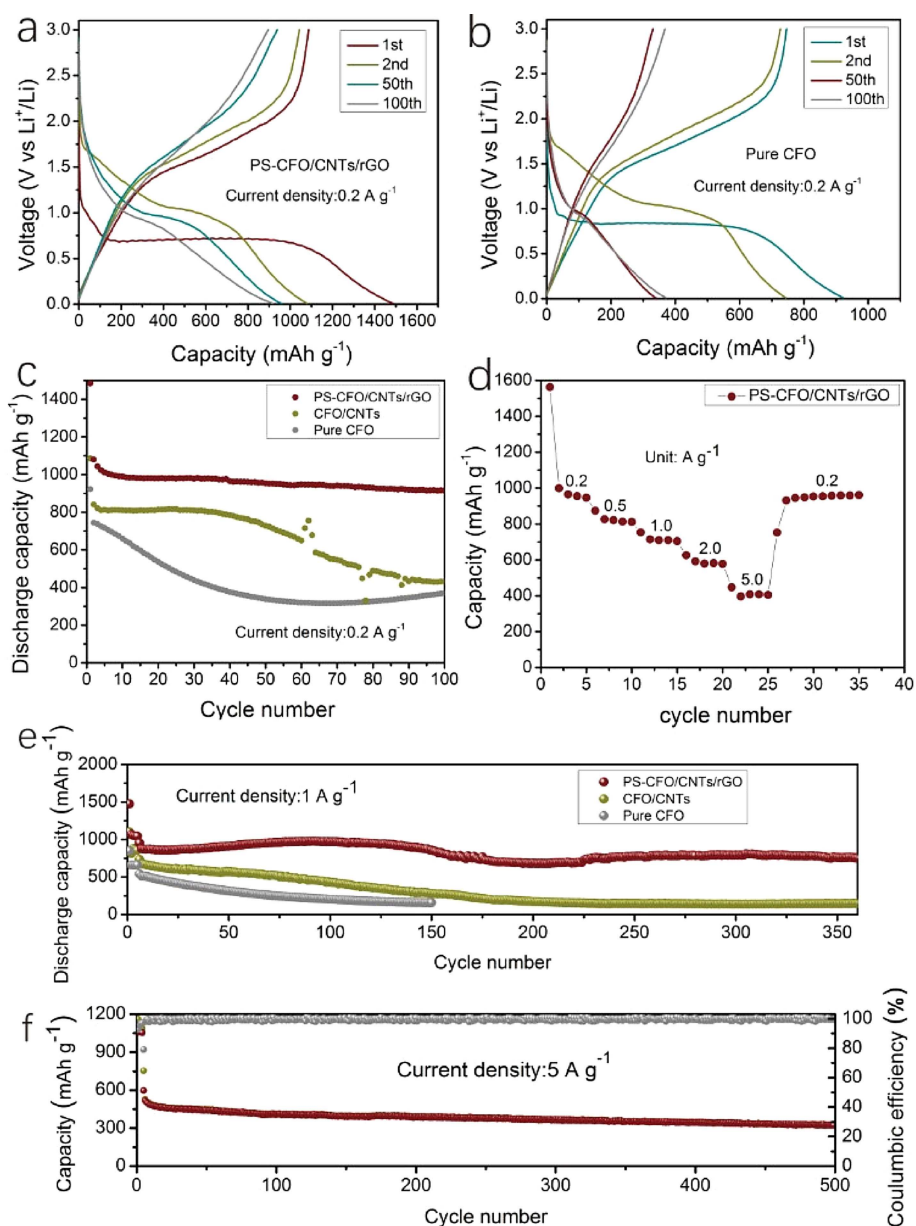


**Figure 4.** Charge-discharge profiles of (a) PS-CFO/CNTs/rGO and (b) Pure CFO composites at  $0.2 \text{ A g}^{-1}$ . (c) Cycling performances of the three samples at  $0.2 \text{ A g}^{-1}$ . (d) Rate performance of PS-CFO/CNTs/rGO composite at different current densities. (e) Long-term cycling performances of PS-CFO/CNTs/rGO, CFO/CNTs and Pure CFO composites at  $1 \text{ A g}^{-1}$  and (f) PS-CFO/CNTs/rGO at  $5 \text{ A g}^{-1}$ . (activated at  $0.2 \text{ A g}^{-1}$  in the first 5 cycles)

CFO composites at  $0.2 \text{ A g}^{-1}$ . After 100 cycles, the capacity of Pure CFO decays to  $370 \text{ mAh g}^{-1}$ , and the CFO/CNTs decays to  $432 \text{ mAh g}^{-1}$ , while the PS-CFO/CNTs/rGO remains at  $916 \text{ mAh g}^{-1}$ . Obviously, the cycling stability of PS-CFO/CNTs/rGO composite is greatly improved compared with that of Pure CFO and CFO/CNTs. When the current density changes from 0.2 to 0.5, 1, 2 and  $5 \text{ A g}^{-1}$ , the capacity of PS-CFO/CNTs/rGO composite is 950, 815, 710, 580 and  $410 \text{ mAh g}^{-1}$  (Figure 4d), respectively. When it recovers to  $0.2 \text{ A g}^{-1}$ , the capacity immediately restores to  $950 \text{ mAh g}^{-1}$ . Meanwhile, for the practical applications of LIBs, long-term cycling properties are also very important. After 365 cycles at  $1 \text{ A g}^{-1}$  (Figure 4e), the discharge specific capacity of PS-CFO/CNTs/rGO stays around

$750 \text{ mAh g}^{-1}$  while the CFO/CNTs decays quickly to  $150 \text{ mAh g}^{-1}$ . And in the first 100 cycles, the discharge capacity of PS-CFO/CNTs/rGO shows a gradual increase. It is caused by the formation of a polymeric gel-like film on the electrode, and the film shows a reversible "pseudocapacitance-type" capacity.<sup>[27]</sup> Then with the continued cycling, due to the damage of the composite structure caused by the volume expansion, the discharge capacity shows a decrease. Moreover, at an extremely high current density of  $5 \text{ A g}^{-1}$  (Figure 4f), after 500 cycles, the stable capacity of PS-CFO/CNTs/rGO electrode remains at  $350 \text{ mAh g}^{-1}$ . And the CEs of PS-CFO/CNTs/rGO composite remain steadily above 99% since the 10th cycle, demonstrating the highly reversible lithiation/delithiation proc-

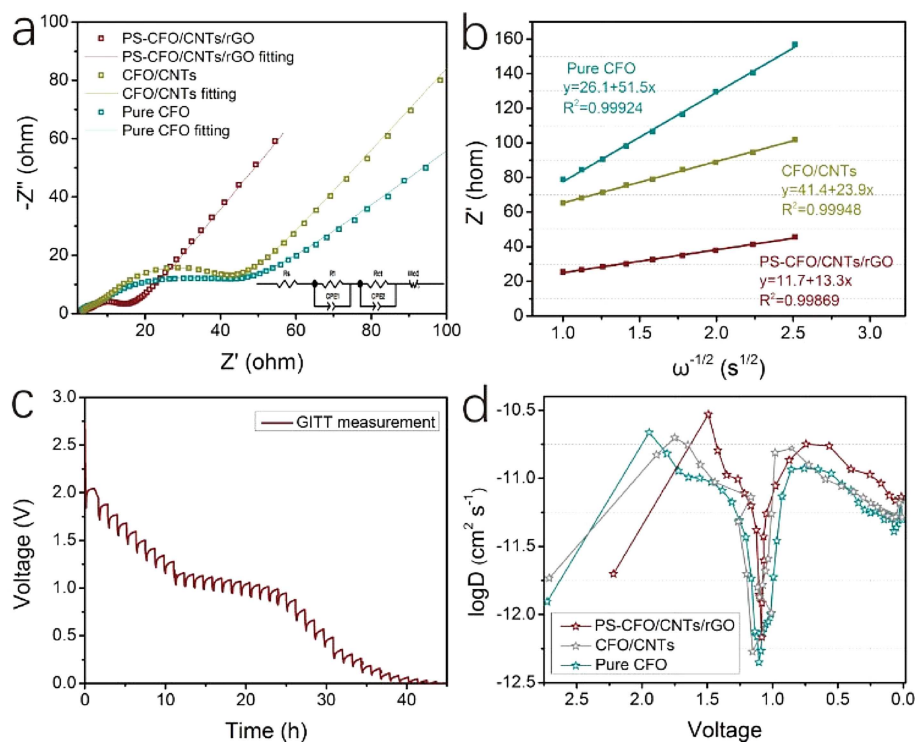


**Figure 5.** (a) EIS of the PS-CFO/CNTs/rGO, CFO/CNTs and Pure CFO electrodes after 5 cycles. (b) The relationship between the reciprocal of the square root of the frequency ( $\omega^{-1/2}$ ) and the real impedance ( $Z'$ ). (c) GITT measurement of PS-CFO/CNTs/rGO electrode. (d) The calculated  $\text{Li}^+$  diffusion coefficients of the PS-CFO/CNTs/rGO, CFO/CNTs and Pure CFO electrodes from GITT curve.

esses. Figure S5 shows the cycling performances of the five samples, demonstrating the influences of carbon materials and the honeycomb structure further.

The superior electrochemical performances of the PS-CFO/CNTs/rGO ternary composite may relate to the enhanced electrode kinetics. Therefore, we have investigated the charge storage mechanism and  $\text{Li}^+$  diffusion behaviors of these three samples. Figure 5a shows the Nyquist curves of PS-CFO/CNTs/rGO, CFO/CNTs and Pure CFO electrodes after 5 cycles. These electrodes fabricated in coin cells are tested from 0.01 Hz to 100 kHz, respectively. The equivalent electrochemical circuit is used to fit the curves (inset of Figure 5a). The  $R_s$ ,  $R_1$ ,  $R_{ct}$ , and  $W_0$  represent the electrolyte resistance, SEI film resistance, charge-transfer resistance, and Warburg impedance, respectively. As shown in the Table 1,  $R_1$  and  $R_{ct}$  of the PS-CFO/CNTs/rGO composite are smaller than that of the Pure CFO and CFO/CNTs composite apparently. It proves that the introduction of the rGO and the hollow porous structure design can improve the charge transfer process of the PS-CFO/CNTs/rGO electrode.

**Table 1.**  $R_1$ ,  $R_{ct}$ ,  $A_w$  and  $D_{\text{Li}^+}$  of the PS-CFO/CNTs/rGO, CFO/CNTs and Pure CFO composites electrodes after 5 cycles.

Sample	$R_1$ ( $\Omega$ )	$R_{ct}$ ( $\Omega$ )	$A_w$ ( $\Omega \text{ s}^{-1/2}$ )	$D_{\text{Li}^+}$ ( $\text{cm}^2 \text{ s}^{-1}$ )
PS-CFO/CNTs/GO	2.2	5.91	13.3	$3.12 \times 10^{-13}$
CFO/CNTs	5.4	32.21	23.9	$0.97 \times 10^{-13}$
Pure CFO	2.1	36.92	51.5	$2.08 \times 10^{-14}$

Meanwhile, the  $\text{Li}^+$  diffusion coefficient has been also calculated to further investigate the electrode kinetics. And the following Eq. 4 shows the calculation method of the  $\text{Li}^+$  diffusion coefficient ( $D_{\text{Li}^+}$ ):

$$D_{\text{Li}^+} = \frac{R^2 T^2}{2A^2 n^4 F^4 C_0^2 A_w^2} \quad (4)$$

In the Eq 4,  $R$  is the gas constant,  $T$  is the absolute temperature,  $A$  is the electrode surface area,  $n$  is the total number of electrons,  $F$  is the Faraday's constant,  $C_0$  is the concentration of  $\text{Li}^+$ , and  $A_w$  is the Warburg factor. And by computing the slope of the line of  $Z'$  versus  $\omega^{-1/2}$  as shown in Figure 5b, the value of  $A_w$  can be obtained. And it relates to  $Z'$  through Eq 5.

$$Z' = R_D + R_L + A_w \omega^{-1/2} \quad (5)$$

The calculated results of  $D_{\text{Li}^+}$  are shown in the Table 1. It is obvious that the PS-CFO/CNTs/rGO composite displays much higher diffusion coefficient than both CFO/CNTs and Pure CFO.

The GITT is a powerful technology to measure  $\text{Li}^+$  diffusion coefficient at different charge state. Figure 5c shows a typical GITT curve of PS-CFO/CNTs/rGO. The battery is discharged with a current impulse of  $20 \text{ mA g}^{-1}$  for an interval  $\tau$  of 10 mins, followed by an open circuit standing for 1 hour. And the  $\text{Li}^+$  diffusion coefficient can also be obtained using GITT data (Eq 6):

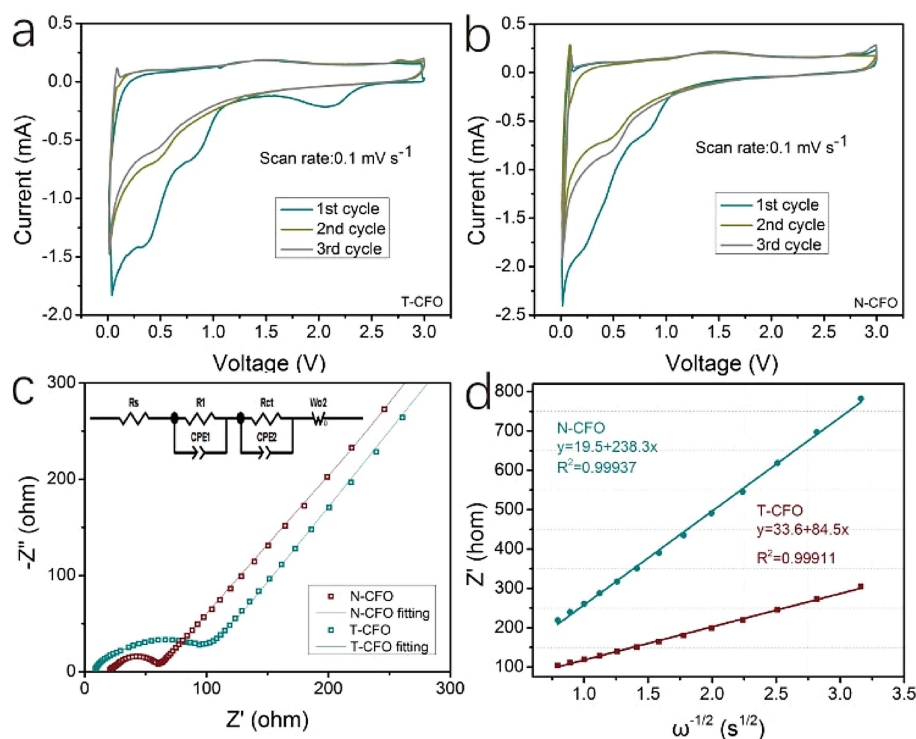


**Figure 6.** (a) CV curves of T-CFO and (b) N-CFO. (c) EIS of the N-CFO and T-CFO after 5 cycles. (d) The relationship between the reciprocal of the square root of the frequency ( $\omega^{-1/2}$ ) and the real impedance ( $Z$ ).

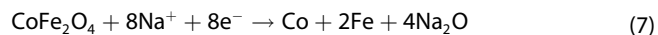
$$D_{GITT} = \frac{4}{\pi\tau} \left( \frac{n_m V_m}{A} \right)^2 \left( \frac{\Delta E_s}{\Delta E_\tau} \right)^2 \left( \tau \ll \frac{L^2}{D_{GITT}} \right) \quad (6)$$

Where  $\tau$  is relaxation time,  $n_m$  is the number of moles,  $V_m$  is the molar volume of  $\text{CoFe}_2\text{O}_4$ ,  $A$  is the surface area of electrode,  $L$  is the thickness of electrode,  $\Delta E_s$  is the change in voltage caused by a pulse,  $\Delta E_\tau$  is the voltage change during a discharge pulse. The  $D_{GITT}$  values of PS-CFO/CNTs/rGO, CFO/CNTs and Pure CFO electrodes are shown in Figure 5d. It is obvious that the value of  $D_{GITT}$  of PS-CFO/CNTs/rGO is greater than that of CFO/CNTs and Pure CFO electrodes. And this result is comparable with the  $D_{Li^+}$  from EIS. It further proves that this honeycomb structure is beneficial to the rapid transport of Li ions.

We have also investigated the electrochemical properties of the PS-CFO/CNTs/rGO composite as the anode of SIBs. However, the PS-CFO/CNTs/rGO electrodes applied in SIBs directly do not show an acceptable electrochemical performance. It is speculated that the radius of sodium ion is larger than lithium ion, which makes the sodiation/desodiation process more difficult, thus increasing the irreversible capacity and volume effect. Although heat-treatment and pre-lithiation treatment on electrodes have been reported to be effective in improving the cycling performance of LIB anode.<sup>[28]</sup> To the best of our knowledge, such methods used in the SIBs are rare. We have successfully developed a facile pre-treatment route applied in SIB anodes combining the heat-treatment and pre-sodiation treatment, which is expected to enhance the electrochemical performance (Figure S6). And we denote the treated and

untreated PS-CFO/CNTs/rGO electrodes as T-CFO and N-CFO, respectively.

Figure 6a and 6b show the CV tests of T-CFO and N-CFO composites in SIBs, respectively. In Figure 6a, several main cathodic peaks are observed at 0.34 and 1.1 V, corresponding to the solid electrolyte interface (SEI) film generation and the reduction of  $\text{Fe}^{3+}$  and  $\text{Co}^{2+}$ . And the weak peak in the anodic sweep at 1.49 V is attributed to the reversible oxidation of  $\text{Fe}^0$  and  $\text{Co}^0$  to  $\text{Fe}^{3+}$  and  $\text{Co}^{2+}$ . We can summarize the electrochemical process of PS-CFO/CNTs/rGO composite in sodium ion batteries in the following equations:



The pretreatment process may have positive impacts on electrode kinetics. Thus, the Nyquist plots of both electrodes after 5 cycles are presented in Figure 6c. The values of  $R_1$  (4.86  $\Omega$ ) and  $R_{ct}$  (32.94  $\Omega$ ) of T-CFO are smaller than that of N-CFO ( $R_1 = 19.93 \Omega$ ,  $R_{ct} = 64.45 \Omega$ ). The  $\text{Na}^+$  diffusion coefficient ( $D_{\text{Na}^+}$ ) can be also calculated in a similar method of  $D_{Li^+}$ . It is evident that  $D_{\text{Na}^+}$  of the T-CFO composite ( $7.74 \times 10^{-15} \text{ cm}^2 \text{ s}^{-1}$ ) is almost an order of magnitude greater than that of the N-CFO composite ( $9.7 \times 10^{-16} \text{ cm}^2 \text{ s}^{-1}$ ) (Figure 6d). The faster charge-transfer process and higher  $\text{Na}^+$  diffusion rate reveal that the pretreatment process can effectively enhance sodiation/desodiation electrode kinetics.

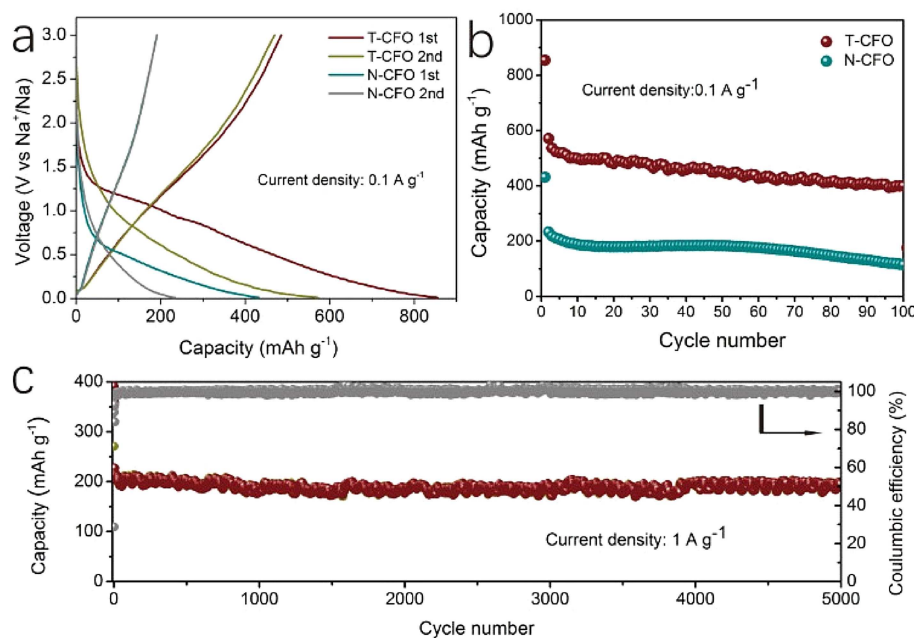


**Figure 7.** Typical charge-discharge curves of (a) T-CFO and N-CFO composites at 0.1 A g<sup>-1</sup>. (b) Discharge capacity retention of T-CFO, N-CFO composites at 0.1 A g<sup>-1</sup>. (c) Long-term cycling properties and CE of T-CFO at 1 A g<sup>-1</sup>.

Figure 7a shows the typical charge-discharge curves of N-CFO and T-CFO composites at 0.1 A g<sup>-1</sup>. The initial discharge specific capacity of T-CFO (854 mAh g<sup>-1</sup>) is higher than that of N-CFO (425 mAh g<sup>-1</sup>). Meanwhile, after 100 cycles, the discharge specific capacity of T-CFO maintains about 400 mAh g<sup>-1</sup> (Figure 7b). More importantly, the cell is further tested at 1 A g<sup>-1</sup> (Figure 7c), the capacity maintains at 195 mAh g<sup>-1</sup> even after 5000 cycles. And the CE approaches 100%, which is good for the ultralong cycling life.

This result further proves the heat-treatment and pre-sodiation treatment can improve the electrochemical performances of PS-CFO/CNTs/rGO electrodes. Apparently, heating electrodes above the melting temperature (170 °C) of the PVDF-HFP binder can redistribute and unfurl long chains to improve electrical contact between active material and conductive additive.<sup>[28a]</sup> And pre-sodiation treatment can introduce sodium source in advance to reduce the irreversible capacity and improve the ICE.<sup>[28b]</sup>

We have also compared our work with other previously reported Co/Fe oxides-based electrodes for LIBs and other metal oxides as the anodes of SIBs. (Table S1, S2) It can be seen that the electrochemical performance of PS-CFO/CNTs/rGO composite is superior when cycling stability, rate performance and reversible capacity are comprehensively considered. The remarkable electrochemical performance of PS-CFO/CNTs/rGO may be due to the following advantages: (1) the honeycomb structure shortens the diffusion path of Li<sup>+</sup>. (2) The rGO coating mitigates the volume effect, and avoids the direct contact between the CoFe<sub>2</sub>O<sub>4</sub> and electrolyte.<sup>[15]</sup> (3) The pre-treatment on electrode can enhance the electrode kinetics in the Na-ion battery.

### 3. Conclusions

In summary, a PS-CFO/CNTs/rGO ternary metal oxide is prepared by the simple spray drying method assisted by polystyrene (PS) soft template, which can be used for both LIBs and SIBs as anode material. And this composite shows excellent electrochemical performances in capacity retention and long-term cycling. At the current density of 1 A g<sup>-1</sup>, the discharge capacity of composite is maintained at 750 mAh g<sup>-1</sup> after 365 cycles for the LIB, and maintained at 195 mAh g<sup>-1</sup> after 5000 cycles for the SIB. In particular, in the preparation of anode material for the SIB, the pre-heating and the pre-sodiation treatment are adopted, which can effectively improve the reversible capacity and cycle stability of electrodes. This strategy is suitable for other metal oxide anodes of SIBs, and it deserves further research.

### Experimental Section

#### Synthesis of PS-CFO/CNTs/rGO

Typically, styrene was washed with 4 mol L<sup>-1</sup> sodium hydroxide solution of the same volume by using a separation funnel to remove the polymerization inhibitor, then washed repeatedly with deionized water until PH=7.0. Next, ethanol-water solution (140 mL), potassium persulfate (0.305 g) and sodium lauryl sulfate (0.152 g) were all added to a three-necked flask. Then heated the solution to 70 °C and continue stirring for 30 mins in the protection of nitrogen atmosphere. After 10 minutes, the 7.0 mL treated styrene was put into the above mixed solution rapidly, and continue stirring for ten hours to obtain the final PS emulsion.<sup>[29]</sup>

In general, to form a uniform dispersion solution, 1 g GO was added in 500 mL ultra-pure water by ultrasonic dispersion. Next, 2.69 g Fe(NO<sub>3</sub>)<sub>3</sub>·9 H<sub>2</sub>O, 0.97 g Co(NO<sub>3</sub>)<sub>2</sub>·6 H<sub>2</sub>O, 20 mL PS emulsion, 2 g CNTs suspension (10 wt%) and 125 mL GO solution were dispersed in 80 mL H<sub>2</sub>O. After stirring for 3 h, the uniform precursor solution was obtained, and the precursor solution was spray-dried (BUCHI Mini Spray Dryer B-290) under 205 °C with 10% pump rate. Then the dried powder was heated to 600 °C for 10 h in the atmosphere of Ar, and the PS-CFO/CNTs/rGO composite was obtained. For comparison, the pristine CoFe<sub>2</sub>O<sub>4</sub> (denoted as Pure CFO), CoFe<sub>2</sub>O<sub>4</sub>/CNTs (denoted as CFO/CNTs), CoFe<sub>2</sub>O<sub>4</sub>/rGO (denoted as CFO/rGO), CoFe<sub>2</sub>O<sub>4</sub>/rGO/CNTs (denoted as CFO/CNTs/rGO) were synthesized in the absence of corresponding carbon materials and PS emulsion solution under the same preparation process.

## Materials Characterization

The field emission scanning electron microscopy (FE-SEM, S-4800, HITACHI) and high-resolution transmission electron microscopy (HRTEM, JEOL-2100) were used to observe the morphology of the composite. The XRD measurements (Rigaku Ultima IV) were tested at a scanning rate of 5° min<sup>-1</sup> from 10 to 90°. And the Raman spectra were gained on Renishaw (Horiba-Jobin Yvon, Japan). The thermogravimetric analysis (TGA, sdt-q600) was conducted from 25 °C to 800 °C under air atmosphere. The N<sub>2</sub> adsorption-desorption was measured by Micromeritics ASAP 2020 (BET).

## Electrochemical Measurement

For the Li-ion batteries, to prepare the working electrodes, the active material, acetylene black (AB), and LA132 binder were grinded, stirred and uniformly mixed to obtain slurry with a mass ratio of 7:2:1. And then coated it to the Copper foil and dried in a vacuum oven at 80 °C overnight. The typical loading mass of active materials in working electrodes was about 1.1 mg cm<sup>-2</sup>. And the specific capacity is calculated based on the total mass of the as-synthesized composite. The typical 2016-type coin cells were assembled to examine the electrochemical performances with lithium foil as the counter electrode and reference electrode. The LiPF<sub>6</sub> (1.0 M) in the diethyl carbonate (DEC) and ethylene carbonate (EC) (v/v = 1: 1) mixture was used as the electrolyte, and the Celgard 2400 was used as the separator. For Na-ion batteries, the same process above was adopted to prepare the working electrodes, except the polyvinylidene fluoride-hexafluoropropylene (PVDF-HFP) was used as the binder. The 1.0 M NaClO<sub>4</sub> in DEC / EC (v/v = 1: 1) was adopted as the electrolyte, and the glass fiber filter was used as the separator. The electrochemical performances for SIBs were tested in the 2032-type coin cells with sodium foil as the counter electrode and reference electrode. All cells were assembled in an Ar-filled glove box. The Solartron was used to test electrochemical impedance spectra (EIS) ranging from 10<sup>-2</sup>–10<sup>5</sup> Hz. The CHI 1030 C was used to test the cyclic voltammetry (CV) curves range from 0.01 and 3.00 V at 0.1 mVs<sup>-1</sup>. The charge-discharge tests and galvanostatic intermittent titration technique (GITT) tests were tested on the Neware CT-3008 W.

## Acknowledgements

The authors gratefully acknowledge financial support from National Key Research and Development Program of China (2017YFB0102000), National Natural Science Foundation of China (21603179, 21621091), the Fundamental Research Funds for the Central Universities (20720170021). The authors also would like to

thank Prof. Daiwei Liao of Xiamen University for his valuable guidance and suggestion.

## Conflict of Interest

The authors declare no conflict of interest.

**Keywords:** CoFe<sub>2</sub>O<sub>4</sub> · spray drying · anode material · lithium-ion batteries · sodium-ion batteries

- [1] a) M. V. Reddy, G. V. Subba Rao, B. V. R. Chowdari, *Chem. Rev.* **2013**, *113*, 5364–5457; b) X. B. Cheng, R. Zhang, C. Z. Zhao, Q. Zhang, *Chem. Rev.* **2017**, *117*, 10403–10473.
- [2] a) J. B. Goodenough, *Energy Storage Mater.* **2015**, *1*, 158–161; b) H. Wang, T. Zhou, D. Li, H. Gao, G. Gao, A. Du, H. Liu, Z. Guo, *ACS Appl. Mater. Interfaces* **2017**, *9*, 4320–4325; c) C. Wang, H. Su, Y. Ma, D. Yang, Y. Dong, D. Li, L. Wang, Y. Liu, J. Zhang, *ACS Appl. Mater. Interfaces* **2018**, *10*, 28679–28685.
- [3] M. Que, Y. Tong, G. Wei, K. Yuan, J. Wei, Y. Jiang, H. Zhu, Y. Chen, *J. Mater. Chem. A* **2016**, *4*, 14132–14140.
- [4] R. L. Sacci, J. M. Black, N. Balke, N. J. Dudney, K. L. More, R. R. Unocic, *Nano Lett.* **2015**, *15*, 2011–2018.
- [5] a) B. Dunn, H. Kamath, J. M. Tarascon, *Science* **2011**, *334*, 928–935; b) J. B. Goodenough, K. S. Park, *J. Am. Chem. Soc.* **2013**, *135*, 1167–1176; c) Z. Yang, J. Zhang, M. C. Kintner-Meyer, X. Lu, D. Choi, J. P. Lemmon, J. Liu, *Chem. Rev.* **2011**, *111*, 3577–3613.
- [6] N. Yabuuchi, K. Kubota, M. Dahbi, S. Komaba, *Chem. Rev.* **2014**, *114*, 11636–11682.
- [7] H. Kang, Y. Liu, K. Cao, Y. Zhao, L. Jiao, Y. Wang, H. Yuan, *J. Mater. Chem. A* **2015**, *3*, 17899–17913.
- [8] H. Pan, Y.-S. Hu, L. Chen, *Energy Environ. Sci.* **2013**, *6*, 2338.
- [9] F. Fu, J. Li, Y. Yao, X. Qin, Y. Dou, H. Wang, J. Tsui, K.-Y. Chan, M. Shao, *ACS Appl. Mater. Interfaces* **2017**, *9*, 16194–16201.
- [10] a) K. Wu, D. Liu, Y. Tang, *Electrochim. Acta* **2018**, *263*, 515–523; b) Y. Kim, K. H. Ha, S. M. Oh, K. T. Lee, *Chem. Eur. J.* **2014**, *20*, 11980–11992.
- [11] Y. Yang, J. Huang, J. Zeng, J. Xiong, J. Zhao, *ACS Appl. Mater. Interfaces* **2017**, *9*, 32801–32811.
- [12] T. Li, X. Bai, Y.-X. Qi, N. Lun, Y.-J. Bai, *Electrochim. Acta* **2016**, *222*, 1562–1568.
- [13] J. Yue, X. Gu, L. Chen, N. Wang, X. Jiang, H. Xu, J. Yang, Y. Qian, *J. Mater. Chem. A* **2014**, *2*, 17421–17426.
- [14] Y. Dong, Y.-S. Chui, X. Yang, R. Ma, J.-M. Lee, J. A. Zapien, *ChemElectroChem* **2015**, *2*, 1010–1018.
- [15] a) T. Li, X. Li, Z. Wang, H. Guo, Y. Li, *J. Mater. Chem. A* **2015**, *3*, 11970–11975; b) P. Kollu, P. R. Kumar, C. Santosh, D. K. Kim, A. N. Grace, *RSC Adv.* **2015**, *5*, 63304–63310; c) L. Wang, K. Zhang, Z. Hu, W. Duan, F. Cheng, J. Chen, *Nano Res.* **2013**, *7*, 199–208.
- [16] H. Xia, D. Zhu, Y. Fu, X. Wang, *Electrochim. Acta* **2012**, *83*, 166–174.
- [17] A. K. Rai, J. Gim, T. V. Thi, D. Ahn, S. J. Cho, J. Kim, *J. Phys. Chem. C* **2014**, *118*, 11234–11243.
- [18] W. Liu, Y. Fu, Y. Li, S. Chen, Y. Song, L. Wang, *Compos. Pt. B-Eng.* **2019**, *163*, 464–470.
- [19] a) Z. Wang, R. T. Downs, V. Pischedda, R. Shetty, S. K. Saxena, C. S. Zha, Y. S. Zhao, D. Schiferl, A. Waskowska, *Phys. Rev. B* **2003**, *68*; b) Y. Qu, H. Yang, N. Yang, Y. Fan, H. Zhu, G. Zou, *Mater. Lett.* **2006**, *60*, 3548–3552.
- [20] a) P. Chandramohan, M. P. Srinivasan, S. Velmurugan, S. V. Narasimhan, *J. Solid State Chem.* **2011**, *184*, 89–96; b) H. Bakhshi, A. Shokuhfar, S. S. S. Afghahi, *Ceram. Int.* **2015**, *41*, 10736–10744.
- [21] Z. Zhu, F. Cheng, J. Chen, *J. Mater. Chem. A* **2013**, *1*, 9484–9490.
- [22] a) L. Zhang, T. Wei, Z. Jiang, C. Liu, H. Jiang, J. Chang, L. Sheng, Q. Zhou, L. Yuan, Z. Fan, *Nano Energy* **2018**, *48*, 238–247; b) Q. He, K. Rui, C. Chen, J. Yang, Z. Wen, *ACS Appl. Mater. Interfaces* **2017**, *9*, 36927–36935.
- [23] C. Nithya, S. Gopukumar, *ChemSusChem* **2013**, *6*, 898–904.
- [24] X. Liu, N. Wu, C. Cui, P. Zhou, Y. Sun, *J. Alloys Compd.* **2015**, *644*, 59–65.
- [25] a) W. Qi, P. Li, Y. Wu, H. Zeng, L. Hou, C. Kuang, P. Yao, S. Zhou, *Prog. Nat. Sci.* **2016**, *26*, 498–502; b) J. Wang, G. Yang, L. Wang, W. Yan, W. Wei, *J. Alloys Compd.* **2017**, *693*, 110–117.
- [26] a) R. Alcantara, M. Jaraba, P. Lavela, J. L. Tirado, *Chem. Mater.* **2002**, *14*, 2847–2848; b) Y. Wang, D. Su, A. Ung, J. H. Ahn, G. Wang, *Nano-*

- technology* **2012**, *23*, 055402; c) Y. Sharma, N. Sharma, G. V. S. Rao, B. V. R. Chowdari, *J. Mater. Chem.* **2009**, *19*, 5047.
- [27] a) D. Bresser, E. Paillard, R. Kloepsch, S. Krueger, M. Fiedler, R. Schmitz, D. Baither, M. Winter, S. Passerini, *Adv. Energy Mater.* **2013**, *3*, 513–523; b) S. Laruelle, S. Grugeon, P. Poizot, M. Dolle, L. Dupont, J. M. Tarascon, *J. Electrochem. Soc.* **2002**, *149*, A627–A634; c) F. Ma, A. Yuan, J. Xu, *ACS Appl. Mater. Interfaces* **2014**, *6*, 18129–18138.
- [28] a) J. Li, L. Christensen, M. N. Obrovac, K. C. Hewitt, J. R. Dahn, *J. Electrochem. Soc.* **2008**, *155*, A234–A238; b) N. Liu, L. Hu, M. T. McDowell, A. Jackson, Y. Cui, *ACS Nano* **2011**, *5*, 6487–6493.
- [29] Y. Yang, J. Li, J. Huang, J. Huang, J. Zeng, J. Zhao, *Electrochim. Acta* **2017**, *247*, 771–778.

Manuscript received: May 12, 2019  
Revised manuscript received: June 5, 2019  
Accepted manuscript online: June 13, 2019